RESEARCH ARTICLE
SOLID EARTH: SEISMOLOGY

Earth and Planetary Physics
8: 535–548, 2024
doi: 10.26464/epp2024022

The 2023 Turkey earthquake doublet: Earthquake relocation, seismic tomography, and stress field inversion

HuiLi Zhan[1,2], Ling Bai[1,2*], Bagus Adi Wibowo[1,2,3], ChaoYa Liu[1,2], Kazuo Oike[4], and Yuzo Ishikawa[5]

[1]State Key Laboratory of Tibetan Plateau Earth System, Environment and Resources (TPESER), Institute of Tibetan Plateau Research, Chinese Academy of Sciences, Beijing 100101, China;

[2]University of Chinese Academy of Sciences, Beijing 100049, China;

[3]Center of Earthquake and Tsunami, Agency of Meteorology, Climatology and Geophysics, Jakarta 10610, Indonesia;

[4]University of Shizuoka, Shizuoka 422-8526, Japan;

[5]Shizuoka University, Shizuoka 422-8529, Japan

Key Points:

- The East Anatolian Fault and Sürgü Fault exhibited steep dip angles, with the East Anatolian Fault slightly oriented toward the southeast for the M_W 7.8 earthquake and the Sürgü Fault slightly dipping toward the north for the M_W 7.5 earthquake.
- The East Anatolian Fault Zone exhibits large-scale low P-wave velocity anomalies. The aftershocks occurred either close to the boundary of the low and high P-wave velocity anomaly zones or within the low P-wave velocity anomaly zones.
- The stress field in the northeastern study area was predominantly characterized by shear stress, whereas the southwestern region exhibited additional strike-slip and tensile stresses.

Citation: Zhan, H. L., Bai, L., Wibowo, B. A., Liu, C. Y., Oike, K., and Ishikawa, Y. (2024). The 2023 Turkey earthquake doublet: Earthquake relocation, seismic tomography, and stress field inversion. *Earth Planet. Phys.*, *8*(3), 535–548. http://doi.org/10.26464/epp2024022

Abstract: On February 6, 2023, two earthquakes with magnitudes of M_W 7.8 and M_W 7.5 struck southeastern Turkey, causing significant casualties and economic losses. These seismic events occurred along the East Anatolian Fault Zone, a convergent boundary between the Arabian Plate and the Anatolian Subplate. In this study, we analyze the M_W 7.8 and M_W 7.5 earthquakes by comparing their aftershock relocations, tomographic images, and stress field inversions. The earthquakes were localized in the upper crust and exhibited steep dip angles. Furthermore, the aftershocks occurred either close to the boundaries of low and high P-wave velocity anomaly zones or within the low P-wave velocity anomaly zones. The East Anatolia Fault, associated with the M_W 7.8 earthquake, and the Sürgü Fault, related to the M_W 7.5 earthquake, predominantly experienced shear stress. However, their western sections experienced a combination of strike-slip and tensile stresses in addition to shear stress. The ruptures of the M_W 7.8 and M_W 7.5 earthquakes appear to have bridged a seismic gap that had seen sparse seismicity over the past 200 years prior to the 2023 Turkey earthquake sequence.

Keywords: Turkey earthquake doublet; earthquake relocation; seismic tomography; stress field; seismicity

---

1. Introduction

On February 6, 2023, southeastern Turkey experienced two devastating earthquakes, resulting in extensive damage and a high death toll (Figure 1). The first earthquake, with a moment magnitude (M_W) of 7.8 occurred at 4:17:36 local time (1:17:36 Coordinated Universal Time [UTC]), followed by a second earthquake with a magnitude of 7.5 that occurred 9 hours later at 13:24:49 local time (10:24:49 UTC). The two earthquakes are referred hereafter to as the 2023 Turkey earthquake doublet (Dal Zilio and Ampuero, 2023; Naddaf, 2023; United States Geological Survey [USGS], 2023). Within 5 months of the earthquake doublet, 3,707 earthquakes of $M_W \geq 3.0$ were recorded (Disaster and Emergency Management Presidency of Turkey [AFAD], 2023). The ruptures occurred at depths of 0–20 km and affected densely populated areas, including the plains of Gaziantep, Kahramanmaraş, and Hatay in the west and the mountainous areas of Adiyaman and Malatya in the east.

The Anatolian Subplate, situated in the convergence zone of the Eurasian, African, and Arabian Plates (Hatzfeld and Molnar, 2010; Abdulnaby et al., 2014), is demarcated by the northeast–southwest-oriented East Anatolian Fault Zone (EAFZ; Ambraseys, 1989; Reilinger et al., 2006). Despite the lack of significant crustal thickening beneath the Anatolian Subplate, a tilt exists in the Moho depth from 40 km in the southwest to 47 km in the northeast along the EAFZ (Sandvol et al., 2003; Zor et al., 2003). Further investigations have confirmed the presence of distinct low- and high-velocity anomalies in the middle crust and upper mantle

---

First author: H. L. Zhan, zhanhl@itpcas.ac.cn
Correspondence to: L. Bai, bailing@itpcas.ac.cn
Received 20 FEB 2024; Accepted 19 MAR 2024.

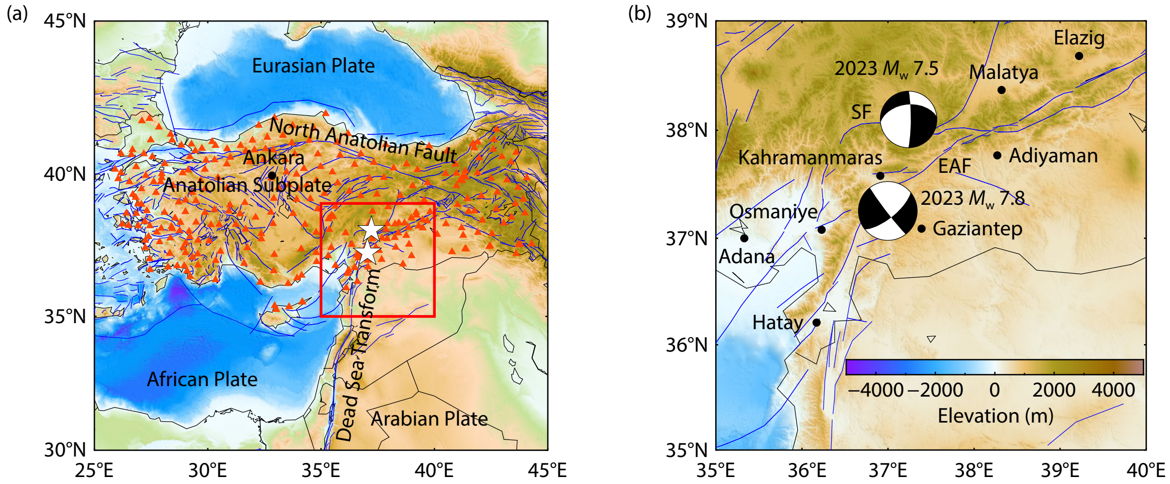

Figure 1. The tectonic background, major faults, and locations of the $M_{\rm W}$ 7.8 and $M_{\rm W}$ 7.5 earthquake doublet that occurred on February 6, 2023, in Turkey. (a) The tectonic background and major faults in Turkey. The stars are the $M_{\rm W}$ 7.8 and $M_{\rm W}$ 7.5 earthquakes. The red triangles are seismic stations (AFAD, 2023). The solid blue lines are active faults (Styron and Pagani, 2020). The red rectangle is the study area. (b) The tectonic background and major faults in the study area. The beachballs are the $M_{\rm W}$ 7.8 and $M_{\rm W}$ 7.5 earthquakes.

(Mutlu and Karabulut, 2011; Wang HB et al., 2020). Moreover, interferometric synthetic aperture radar (InSAR) deformation observations and global navigation satellite system (GNSS) velocity field measurements revealed that the strain accumulation on the Anatolian Subplate averages approximately 30 km (Lloyd, 2014). The slip rate is nearly constant at approximately 10 mm/yr in the northeastern East Anatolian Fault (EAF) and decreases to approximately 4.5 mm/yr in the southwestern EAF (Aktug et al., 2016).

The fault zone was segmented, including the EAF in the south and the Sürgü Fault (SF) in the north, which hosted the $M_{\rm W}$ 7.8 and $M_{\rm W}$ 7.5 earthquakes, respectively (Dal Zilio and Ampuero, 2023; Hall, 2023; https://earthquake.usgs.gov/). The ruptures of these seismic events were characterized as supershear, with displacements reaching up to 6–8 m (Jia Z et al., 2023; Melgar et al., 2023; Meng JN et al., 2024; Ren CM et al., 2024). The interaction between the faults triggered the earthquake doublet (Chen WK et al., 2023) and the alignment of the aftershocks with the rupture zones highlight the complexity of coseismic deformation. Notably, the main faults originated subvertically but exhibit lateral variations (Ding HY et al., 2023). These observations indicate that seismicity and coseismic deformation are intricate, with possible coincident ruptures occurring in different small segments of the fault zone. The concurrence of these events increased stress across several major fault zones in the vicinity, including the East Cyprus Arc, the Dead Sea Fault, and multiple faults in East Anatolia (Karabulut et al., 2023). Investigation of their seismicity and velocity structure is crucial for understanding the characteristics of deep source and the nature and types of stresses affecting the eastern part of the Anatolian Subplate, which are essential for assessing internal deformation.

In this study, we analyzed the $M_{\rm W}$ 7.8 and $M_{\rm W}$ 7.5 earthquakes by comparing earthquake relocations, tomographic imaging, and stress field inversion to elucidate characteristics of the seismic activity in the region. We relocated 3,707 earthquakes of $M_{\rm W} \geq 3.0$ that occurred within 5 months following the $M_{\rm W}$ 7.8 event. Subsequent analysis of seismicity facilitated the examination of both temporal and spatial variations. Additionally, we compiled data on significant earthquakes dating back to 1800 to explore the rupture history along the fault zone. Focal mechanisms of the earthquakes were used for stress field inversion. This research provides new insights into the temporal and spatial patterns of seismicity, the crustal velocity structure, and the lateral variation of the active fault system associated with the 2023 Turkey earthquake doublet.

2. Data and Methods

2.1 Earthquake Arrival Time and Focal Mechanism Data

The Disaster and Emergency Management Presidency of Turkey provides real-time data from more than 700 seismic stations. These stations allow for the identification of direct (Pg and Sg) and head (Pn and Sn) waves at local and regional seismic stations, respectively (Bai L et al., 2019), facilitating the acquisition of accurate earthquake locations (Figure S1). Each earthquake is recorded with at least eight phase records, and time–distance curve fitting is used to ensure the retention of high-quality earthquake arrival times. In the AFAD catalog, many earthquakes have their focal depths fixed at 7 km. From February 6, 2023, to June 20, 2023, we relocated 3,707 earthquakes with $M_{\rm W} \geq 3.0$, including the $M_{\rm W}$ 7.8 and $M_{\rm W}$ 7.5 earthquake doublet. A one-dimensional velocity model, derived from the January 24, 2020, $M_{\rm W}$ 6.8 Doğanyol–Sivrice earthquake sequence (Melgar et al., 2020; Taymaz et al., 2021), was utilized in this relocation.

The focal mechanisms obtained from the Global Centroid Moment Tensor Catalog (gCMT; Dziewonski et al., 1981; Ekström et al., 2012) and the AFAD of Turkey (AFAD, 2023) facilitated the stress field inversion analysis. In the study area, 755 earthquakes of $M_{\rm W}$ ≥ 4.0 and detailed focal mechanisms were recorded between January 1, 1976, and June 5, 2023. According to these catalogs, the seismic events comprised 213 normal-faulting, 46 thrust-faulting, and 496 strike-slip-faulting earthquakes, which were classified based on their strike, slip, and rake angles (Zhou SY and Xu ZH, 2018).

2.2 Methods of Earthquake Relocation, Seismic Tomography, and Stress Field Inversion

We applied the double-difference earthquake relocation algorithm (hypoDD; Waldhauser and Ellsworth, 2000) to refine the accuracy of earthquake locations. This method relies on pairs of earthquakes with small differences in their hypocentral distances relative to the distances between stations, allowing for the precise correlation of spatial shifts between the pairs with the travel time discrepancies observed at individual stations. The hypoDD algorithm systematically reduces the discrepancies between observed and modeled travel times through the adjustment of relative hypocenter locations and the travel time of all paired events and stations. This approach effectively addresses potential inaccuracies resulting from incomplete knowledge of structural complexities along the path from the source to the receiver. In our study, we focused on event pairs within 10 km of each other and ensured a minimum of eight links to stations, resulting in a significant reduction of the average root-mean-square travel time residuals from 0.48 seconds before relocation to 0.13 seconds after relocation (Figures S1b and S1c). Since the introduction of the double-difference relocation method by Waldhauser and Ellsworth (2000), Zhang HJ and Thurber (2003, 2006) have expanded on this foundation to develop the double-difference tomography method. After a series of tests, a damping value of 100 was selected as the most appropriate damping value. We iterated the inversion process 5 times, with 3 iterations for hypocenter relocation, and 2 iterations for simultaneous joint inversion. Subsequently, greater importance was given to the differential arrival times of earthquake pairs, thus enhancing the precision of the velocity structure of the source region (Yao HJ, 2012; Xiao Z and Gao Y, 2017; Shao XH et al., 2022). The checkerboard test (Figures S2, S3, S4), a widely used method for model evaluation introduced by Claerbout (1976), played a crucial role in the inversion process. To ensure that enough ray paths covered the research area, we considered the density of the ray paths based on the derivative weight sum value (Figure S5). After extensive testing, we found that a grid accuracy of 0.25° × 0.25° yielded the most stable results in this region (Figures S2, S3, S4).

For stress field inversion, we applied the methods developed by Hardebeck and Michael (2006), utilizing the MSATSI software suite (Lund and Townend, 2007; Martínez-Garzón et al., 2014). To ensure a stable stress field across the entire region, reasonable damping was introduced to reduce uncertainties caused by the gridding process in the inversion analysis (Figure S6). The optimal orientations of the stress axes and the R values were determined following the approach of Gephart and Forsyth (1984):

$$R = \frac{\sigma_2 - \sigma_1}{\sigma_3 - \sigma_1}, \qquad (1)$$

where σ_1, σ_2, and σ_3 denote the maximum, intermediate, and minimum principal compressive stresses, respectively. An R value approaching 1 signifies that σ_2 and σ_3 exhibit similar tensile stresses, indicating a biaxial tensile state where the two axes are indistinguishable. An R value near 0.5 allows for the identification of all three stress axes, facilitating the classification of the stress field by examining the dip of these axes. Conversely, an R value close to 0 suggests that σ_1 aligns with σ_2, indicating a biaxial compressive state where the axes are indistinguishable (Guiraud et al., 1989; Huang JC et al., 2016; Wan YG et al., 2016; Cui HW et al., 2022).

3. Results

3.1 Earthquake Relocations and Tomographic Images

Within 5 months after the 2023 Turkey earthquake doublet, 2,016 earthquakes of $M_W \geq 3.0$ were relocated in the study area. Utilizing these relocated earthquakes, we generated a map view (Figure 2) and cross-sectional profiles (Figures 3 and 4) of various fault branches. The analysis revealed distinct lateral inhomogeneity in P-wave velocity at different depths (Figure S7), with the EAFZ exhibiting notable low P-wave velocity anomalies. A significant number of earthquakes were situated at the transition areas of high and low P-wave velocity zones or within areas of low P-wave velocity anomalies. Aftershocks were extended bilaterally along the EAF and SF fault lines. Both the M_W 7.8 and M_W 7.5 earthquakes occurred near the central branch of the two faults (Figure 2). Figures 3 and 4 illustrate eight cross-sectional profiles of the EAF and SF (labeled a–a′–a ″, b–b′, c–c′, d–d′, e–e′, f–f′, g–g′, and h–h′

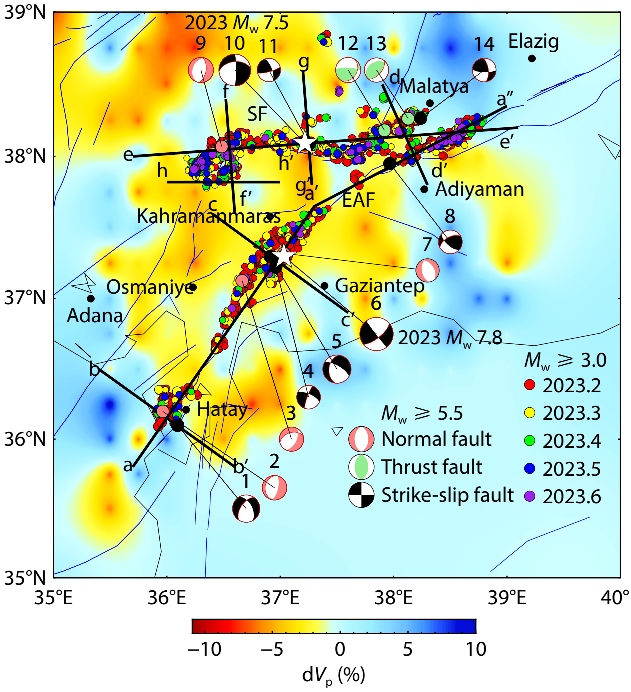

Figure 2. Earthquake activity within 5 months after the 2023 Turkey earthquake doublet and tomographic image at 5 km depth. This figure shows the results of P-wave velocity anomalies at the 5 km depth. Results at additional depths are shown in Figure S7. The black lines are the profile lines a–a′–a″, b–b′, c–c′, d–d′, e–e′, f–f′, g–g′, and h–h′. The focal mechanisms are earthquakes of $M_W \geq 5.5$ (see Table S1 for details) with two possible fault planes. The red line in each focal mechanism indicating the speculated principal fault planes. The red, yellow, green, blue, and purple dots indicate seismic activity in February, March, April, May, and June 2023, respectively.

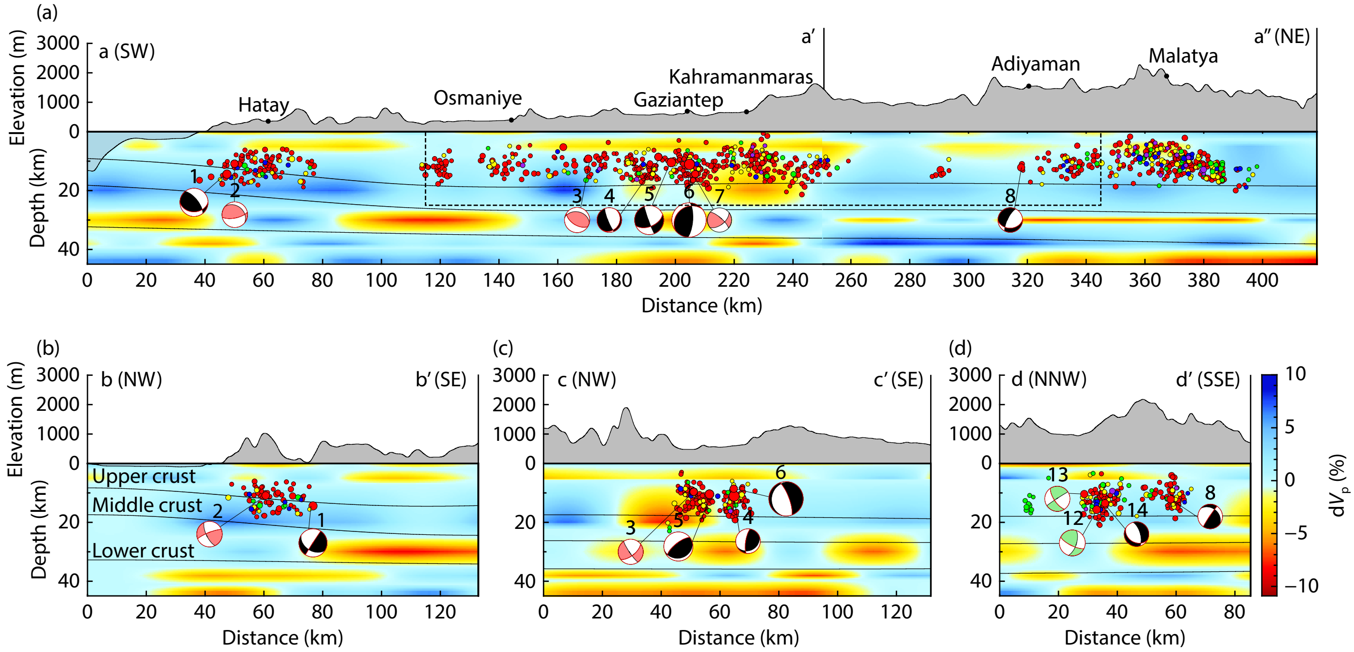

Figure 3. The distribution of aftershocks and the P-wave velocity anomalies along profiles near the EAF.

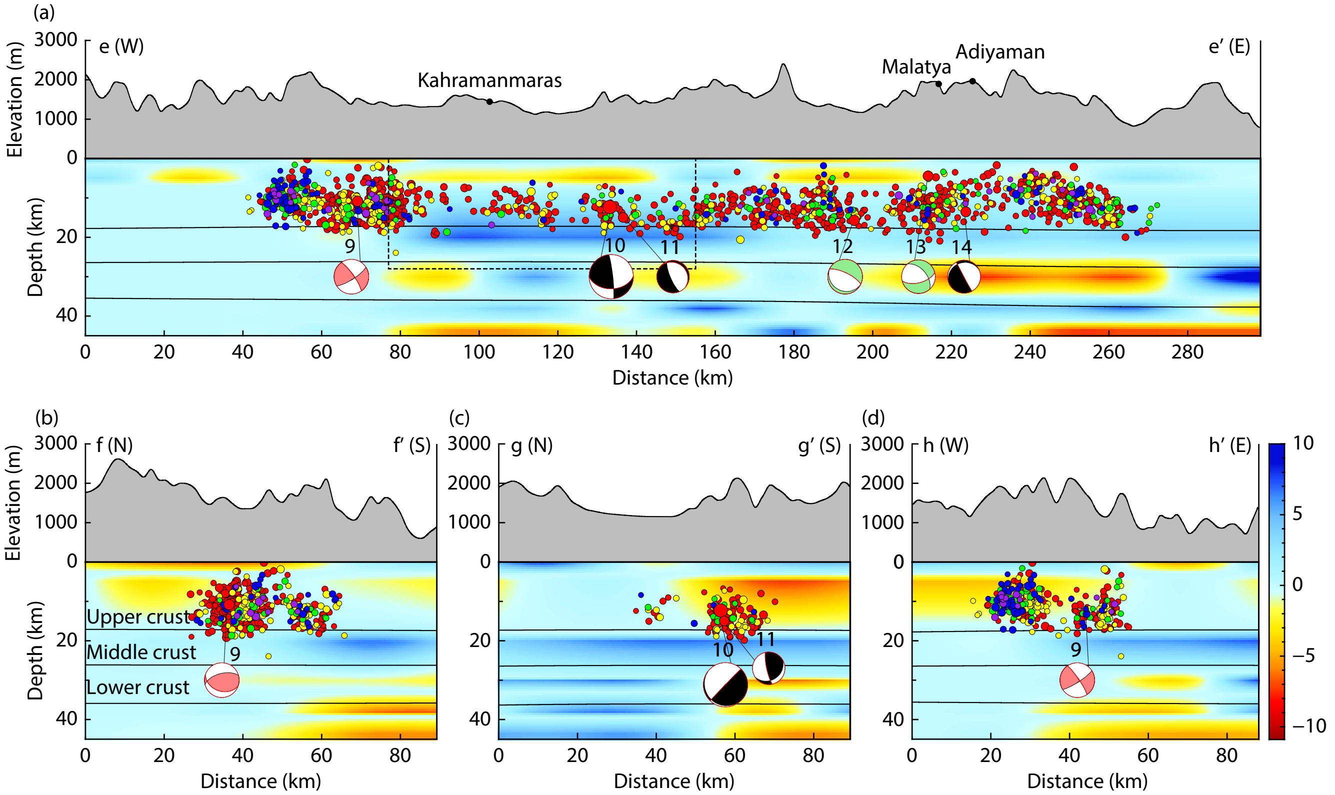

Figure 4. The distribution of aftershocks and the P-wave velocity anomalies along profiles near the SF.

in Figure 2), with earthquake data selected within a 15 km width surrounding these profiles.

Figure 3 illustrates the seismic profiles related to the EAF for the M_W 7.8 earthquake, showing aftershocks predominantly within the 0–20 km depth range, consistent with historical seismicity in the source area (Melgar et al., 2020; Taymaz et al., 2021). The majority of aftershocks were located in the upper crust, with a few in the middle crust near the southwestern end of the Mediterranean Sea. The 400-km-long profile a–a′–a″ revealed greater seismicity in the northeastern segment compared with the southwestern segment. Aftershocks in the northeastern area, covering the Gaziantep, Kahramanmaras, Adiyaman, and Malatya Provinces, culminated in a high P-wave velocity zone. Two seismic clusters had focal depths that deepened gradually from south to north, one stretching from the hypocenter of the M_W 7.8 earthquake to Kahramanmaras, and another extending from Adiyaman to Malatya. Between these clusters, aftershocks were sparse, with the initiated rupture of the M_W 7.5 earthquake in the same longitudinal range. The M_W 7.8 event triggered a deep rupture that stopped near the high and low P-wave velocity boundary and extended approximately 90 km southwest from the epicenter, showing a gradual velocity shift at the southwestern edge of the rupture and no significant aftershock activity beyond this boundary. Conversely, approximately 140 km to the northeast, an increase in aftershocks was noted beyond the northeastern boundary. Profile b–b′ traversed the Hatay region near the Mediterranean Sea, where is 150 km away from the epicenter and the high and low P-wave velocity zones intersect. However, there were still aftershocks two months after the M_W 7.8 event. Profile c–c′ spanned the epicenter of the M_W 7.8 earthquake, indicating that the rupture began along a distinct fault branch directed south-southwest with a nearly vertical dip, distinctly separate from the main EAF branch. Both cross-sectional and longitudinal profiles confirmed that the M_W 7.8 event occurred within a low P-wave velocity anomaly zone, associated with Triassic–Cretaceous (partially ophiolitic) and Plio-Quaternary sediments in the crust (Yilmaz et al., 2006). Profile d–d′ showed consistent seismic activity over time in the Adiyaman and Malatya regions, characterized by a relatively low P-wave velocity. The two distinct earthquake clusters corresponded to seismic activity along the EAF and SF.

The light blue area is the ocean, and the gray area is the continent. The area within the dashed black line indicates the approximate extent of the rupture (Xu CY et al., 2023). The three black lines on the depth profile indicate the upper, middle, and lower crust interfaces, respectively (Laske et al., 2013). Relatively high and low P-wave velocity perturbations are represented by the blue and red colors, respectively. Profile lines (a) a–a′–a″, (b) b–b′, (c) c–c′, and (d) d–d′, as shown in Figure 2.

Figure 4 presents seismic profiles related to the SF for the M_W 7.5 earthquake. The profile e–e′ extends approximately 300 km in the east–west direction, with initial higher seismic activity in the eastern region during February, March, and April, and an increase in the west during May and June (Figure 4a). Seismic activity was notably intense beneath Kahramanmaras Province to the west (Figure 4b), whereas aftershocks at the eastern end of the fault zone were more evenly distributed. The area between the epicenter of the M_W 7.5 earthquake and the Kahramanmaras cluster exhibited sparse seismicity, with supershear rupture propagating westward (Melgar et al., 2023). The rupture of the M_W 7.5 earthquake stopped near the boundary between high and low P-wave velocities, extending about 60 km west and 20 km east along the SF. Profiles f–f′ and h–h′ illustrate aftershock clusters beneath Kahramanmaras (Figures 4b and 4d), showing the migration of aftershocks from north to south along the western SF. Two earthquake clusters were distinguished in the profile h–h′: a primary cluster along the northern SF trend and a secondary, smaller cluster to the south. Profile f–f′ indicated that the aftershocks occurred in a zone of relatively low P-wave velocity, in contrast to other profiles that exhibited a clear transition between high and low P-wave velocities. Profile h–h′, which delineates the western boundary near the SF, showed earthquakes along the high and low P-wave velocity boundary. Profile g–g′ indicated fewer aftershocks near the M_W 7.5 earthquake zone (Figure 4c). The focal mechanism of the M_W 7.5 earthquake suggested a primarily north-dipping fault that occurred in a zone of relatively high P-wave velocity associated with Upper Cretaceous granitic rocks within the crust (Yilmaz et al., 2006). Most of the aftershocks around the M_W 7.5 event were located at the boundary between the high and low P-wave velocity anomalies, highlighting a sharp transition in P-wave velocities throughout the entire depth range of the source area. The southern side, near the source area of the M_W 7.8 earthquake, exhibited low P-wave velocity anomalies.

Other symbols are the same as in Figure 3. Profile lines (a) e–e′, (b) f–f′, (c) g–g′, and (d) h–h′, as shown in Figure 2.

3.2 Stress Field from the Focal Mechanism Inversion

The study area was segmented into 300 stress cells, each measuring 0.25° × 0.25°, based on the analysis of focal mechanism solutions (Figure S6). Each cell was guaranteed to contain at least one focal mechanism, but because stress field inversion requires at least four focal mechanisms, data from adjacent grids were aggregated for stress tensor smoothing. Of the 300 grids, stress fields were successfully calculated for 101 grids. The uncertainty associated with these stress field estimations at the 95% confidence level was determined from 1000 samples of the original dataset (Figure 5d; Hardebeck and Michael, 2006).

Along the EAF, the primary orientation of σ_1 varied between north–south and north-northeast, reflecting the motion of the Arabian Plate relative to the Eurasian Plate. In the northwestern study area, an R value near 0 indicated a biaxial compression state with σ_1 and σ_2 being comparable. At the epicenter of the M_W 7.8 earthquake, a low R value suggested minimal inclination for σ_1, with σ_2 and σ_3 nearly horizontal, indicating combined strike-slip and tensile stresses. Near the epicenter of the M_W 7.5 earthquake, the R value around 0.5 revealed well-defined axis orientations, with σ_1 and σ_3 showing slight inclinations and σ_2 nearly vertical, indicating predominant shear stress in the eastern SF.

Similarly, in the northeastern EAF, the R value close to 0.5, with a steep dip for σ_2 and shallow dips for σ_1 and σ_3, suggested shear stress dominance. The southwestern EAF exhibited an R value around 0.5, with a steep dip for σ_1 and shallower dips for σ_2 and σ_3, indicating tensile stress dominance. In the western SF, an R value near 0 denoted the coexistence of strike-slip and tensile stresses. The varying R values between the EAF and SF highlighted the mixed characteristics of strike-slip, tensile, and compressive stresses.

4. Discussion

4.1 Seismicity and P-wave Velocity Anomalies under the Eastern Anatolian Subplate

The M_W 7.8 and M_W 7.5 earthquakes exhibited a bilateral distribution, with the rupture zones closely aligned with the zones of aftershocks. These seismic events primarily occurred in the upper crust and caused significant damage in the densely populated

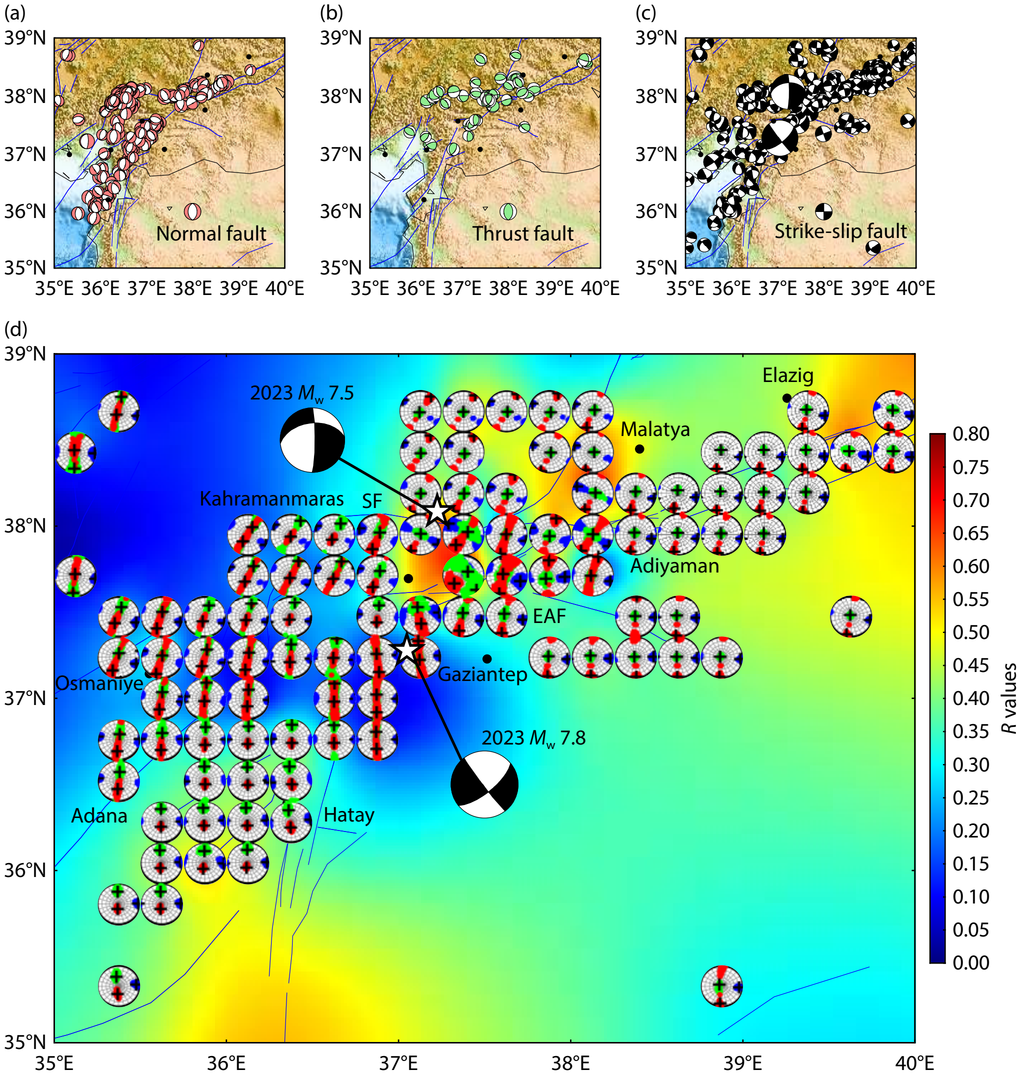

Figure 5. Distribution of focal mechanism solutions (Dziewonski et al., 1981; Ekström et al., 2012; AFAD, 2023) and results of the stress field inversion around the EAF and SF. (a) Pink beachballs represent the normal-faulting mechanisms. (b) Light green beachballs represent the thrust-faulting mechanisms. (c) Black beachballs represent the strike-slip-faulting mechanisms. (d) The red, green, and blue dots represent the resampling of the σ_1, σ_2, and σ_3 axes at a 95% confidence level. The cross symbols represent the optimal solution for each of the compressional axes. The background color represents the *R* value of the stress form factor.

regions of Turkey and Syria. Following the M_W 7.8 event, surface ruptures and aftershocks extended in a northeast–southwest direction. Particularly active aftershocks in the northeast direction formed two clusters, where focal depths progressively deepened toward the northeast, with an average dip angle of approximately 5°. This pattern was consistent with the slight increase in the crustal thickness toward the northeast identified in the source region (Figure 3a; Zor et al., 2003; Laske et al., 2013). The focal mechanism of the M_W 7.8 earthquake demonstrated a high dip angle toward the southeast, with aftershocks near the central rupture branch displaying similar steep dip angles (Figure 3c). The Anatolian Subplate exhibits a lower average crustal shear wave velocity than the global average for continental crust, possibly because of recent volcanic activity or the ascent of hot magma layers through a plate window created by the disintegration of the subducting oceanic Arabian Plate between 11–10 Ma (Warren et al., 2013), or because of elevated temperatures, the presence of fluids, or both (Delph et al., 2015). At the hypocenter of the M_W 7.8 earthquake, the observed low P-wave velocity structure implies that the EAF experienced ductile damage. Along the EAF, low P-wave velocity anomalies beneath Hatay and Adiyaman were associated with significant liquefaction observed at the Gölbaşı lakeshore in Adiyaman, at the İskenderun Port wharf, and near the Asi River in Antakya (Erdik et al., 2023). Notably, the presence of low-velocity anomalies beneath Adiyaman lessened, marked by a single M_W 5.6 strike-slip earthquake to the southwest (no. 8 in Figure 2, occurring at 2:3:35 UTC on February 6, 2023), where field studies indicate the termination of the northeast-directed surface rupture (Karabacak et al. 2023). The fault plane of the M_W 7.5 earthquake was notably steep and the dip was slightly to the north (Figure 4c), coinciding with the high P-wave velocity anomalies identified on the north side of the SF. Along the SF, the majority of earthquakes were located near the boundary of high and low P-wave velocity anomalies, with a preference for the high

P-wave velocity side. Such boundaries, where properties of the medium are influenced by local structural changes, are considered common areas for the initiation and occurrence of large earthquakes (Li DH et al., 2021). At the hypocenter of the M_W 7.5 earthquake, the presence of a relatively high P-wave velocity structure indicates that brittle failure followed stress accumulation within the SF, a process that unfolds swiftly with minimal forewarning, thereby facilitating abrupt seismic occurrences. This situation underscores the likelihood of sudden and devastating seismic events within areas of high P-wave velocity.

4.2 The Dynamic Implications Revealed by the Stress Field and Coseismic Displacement

Regional crustal movement was revealed by the coseismic offset measurements from GNSS, and their joint analysis with tectonic stress fields allowed an in-depth discussion of the dynamic effects of earthquakes (Tian JH et al., 2019). The main direction of the maximum principal compressive stress σ_1, derived from the earthquake focal mechanisms, was predominantly aligned with the north–south and north-northeast directions (Figure 6). This orientation alignment closely matches the coseismic rupture direction of the M_W 7.8 earthquake and reflects the relative motion between the Arabian Plate and the Anatolian Subplate. The minimum principal compressive stress σ_3 was oriented near the east–west and northwest-west directions, reflecting the eastward movement of the Anatolian Subplate amidst the north–south compression. For the M_W 7.8 earthquake, the coseismic displacement recorded by the GNSS station MLY1 reached 0.3 m toward the southwest (Nevada Geodetic Laboratory [NGL], 2023; http://geodesy.unr.edu/). Similarly, large displacement was observed on the SF in the southwest direction (Meng JN et al., 2024), indicating the influence of the M_W 7.8 earthquake on the rupture of the SF. This observation supports the hypothesis that the M_W 7.8 event significantly encouraged the onset of the subsequent M_W 7.5 earthquake because of Coulomb failure (Li SP et al., 2023). For the M_W 7.5 earthquake, the displacement recorded by the GNSS station EKZ1 reached 4.4 m toward the west (NGL, 2023). The northeastern study area exhibited predominantly shear stress, consistent with the northeast and southwest coseismic displacements associated with the earthquake doublet at the intersection of the EAF and SF. Conversely, the southwestern study area was characterized by a high rate of normal-faulting earthquakes, maintaining the same stress state reported by Över et al. (2002). The observed tensile stress and coseismic displacement were likely due to extensional processes resulting from the curvature of the EAF and SF and the westward movement of the Anatolian Subplate relative to the Arabian Plate. Such complex tectonic stresses, accumulated in and around the fault zone, have led to frequent seismic activity in the area (Okuwaki et al., 2023).

For the M_W 7.8 earthquake, ruptures were identified without supershear (Jia Z et al., 2023) or with supershear on the southwestern EAF (Zhang YJ et al., 2023) or the northeastern EAF (Ren CM et al., 2024). Our stress field inversion showed a predominantly tensile tectonic stress field on the southwestern EAF in the range of 35°E–36.5°E and a predominantly shear tectonic stress field on the northeastern EAF in the range of 38°E–40°E (Figure 5). The large ruptures of the M_W 7.8 earthquake were concentrated in the northeastern EAF. These observations suggest that the northeastern EAF was more suitable for generating strike-slip ruptures for the M_W 7.8 earthquake and its aftershocks. Similarly, a supershear rupture was observed in the western SF during the M_W 7.5 earthquake (Jia Z et al., 2023; Melgar et al., 2023; Zhang YJ et al., 2023), and both strike-slip and tensile stresses were observed in this study. The aftershock activity of the western SF was lower compared with the eastern SF, although the tectonic stress types were more complex. In addition, previous studies have defined the fault maturity by the duration of slip activity on a fault, indicating that fault propagation generally progresses from mature to less mature sections (Perrin et al., 2016; Manighetti et al., 2021). The complexity of the tectonic stress field suggests that the fault maturity in the southwestern EAF exceeded that in the western SF. This pattern also implies that the fault rupture after the M_W 7.8 earthquake extended into the area of the M_W 7.5 earthquake.

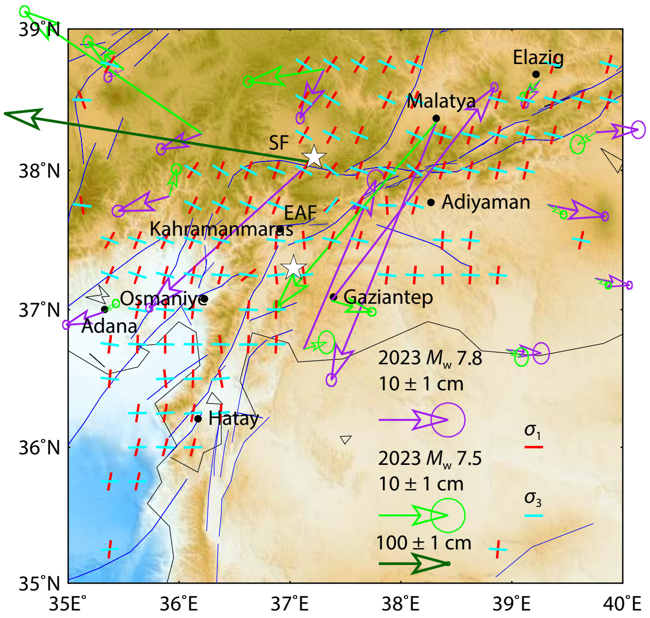

Figure 6. The GNSS coseismic offset measurements for the 2023 earthquake doublet (NGL, 2023) and distribution of the maximum (minimum) principal compressive stress σ_1 (σ_3). The purple arrows indicate the coseismic horizontal displacements of the M_W 7.8 earthquake, and the green arrows indicate the coseismic horizontal displacements of the M_W 7.5 earthquake. The error ellipse indicates the 95% confidence interval. The red lines indicate the σ_1 axis, and the cyan lines indicate the σ_3.

4.3 The Earthquake Doublet in a Long-Term Seismic Gap

The 2023 earthquake doublet in Turkey was anticipated because of the absence of significant seismic events of $M_\mathrm{W} \geq 7.0$ since 1800 within a 300 km historical seismic gap (illustrated by the green dotted ellipse in Figure 7; Karabulut et al., 2023). In particular, an earthquake doublet with magnitudes of M 7.3 and M 7.2 took place at the southwestern gap on April 2 and April 3, 1872. At the northeastern gap, another earthquake doublet, with magnitudes of M 7.1 and M 7.0, occurred on March 2 and March 31, 1893 (Ishikawa, 1986; Utsu, 2002). The rupture length of the M_W 7.8 earthquake appears to have bridged this long-standing seismic

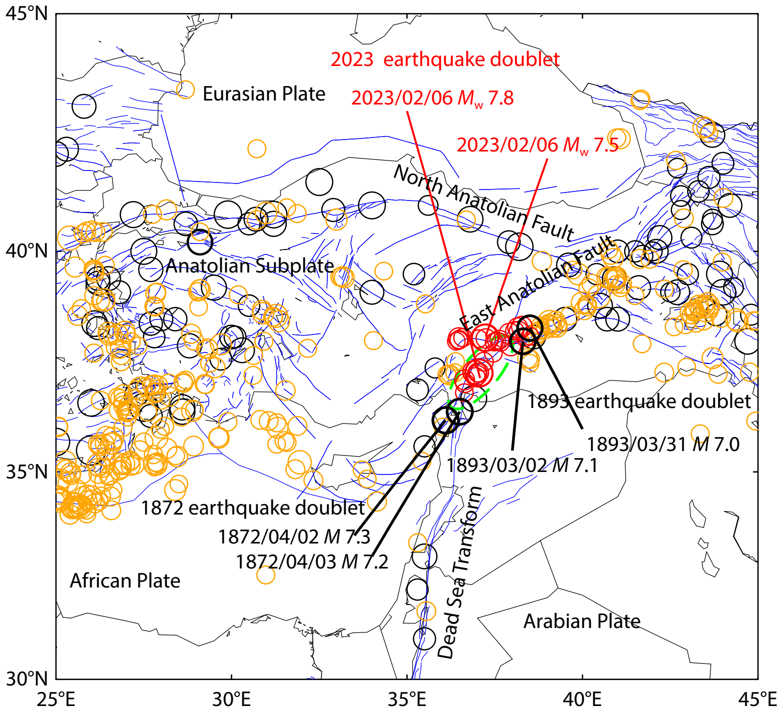

Figure 7. The distribution of historical earthquake doublets, the seismic gap (green ellipse), and large earthquakes since 1800. The black circles represent the distribution of earthquakes with $M \geq 5.0$ from 1800 to 2000 (Utsu, 2002), the orange circles represent the distribution of large earthquakes with $M \geq 5.0$ from 2000 to 2022 (USGS, 2023), and the red circles represent the distribution of large earthquakes with $M \geq 5.0$ in 2023 (AFAD, 2023).

gap (Figure 7). The collision of the Arabian and Indian Plates with the Eurasian Plate created the Zagros–Himalayan seismic belt (Bai L et al., 2017). Notably, the eastern Himalayas experienced an M_S 8.6 earthquake in the Assam area on August 15, 1950, marking the largest inland earthquake ever documented (Zhan HL et al., 2023). The central Himalayas are known to contain a similar seismic gap, highlighting a region prone to significant seismic activity (Khattri, 1987; Bilham et al., 2001; Rahman and Bai L, 2018; Bilham, 2019). Within the east-central Himalayan seismic gap, a pair of earthquakes with magnitudes of M_W 7.8 and M_W 7.3 occurred on April 25 and May 12, 2015, respectively (Bai L et al., 2016, 2019). Given the observed similarities in source parameters between large earthquake doublets occurring within both long-term and short-term seismic gaps, it becomes crucial to conduct a comprehensive investigation of the entire 7000 km Himalayan–Zagros Mountain range to assess the earthquake potential associated with the continental plate convergence zone.

5. Conclusions

In this study, we conducted a comprehensive analysis of the 2023 Turkey earthquake doublet, based on aftershock relocation, seismic tomography, and stress field inversion. The main results are summarized below:

(1) A large number of aftershocks were located in the upper crust. The EAF and the SF demonstrated steep dip angles, with the EAF slightly oriented toward the southeast for the M_W 7.8 earthquake, and the SF-inclined dip to the north for the M_W 7.5 earthquake.

(2) The EAFZ is characterized by low P-wave velocity anomalies, with many earthquakes located at the boundary of high and low P-wave velocity zones or within low P-wave velocity anomalies. The M_W 7.8 earthquake took place in an area with a low P-wave velocity zone associated with slow ductile deformation, whereas the M_W 7.5 earthquake occurred in a high P-wave velocity zone associated with brittle deformation.

(3) Inversion of the tectonic stress field and observations of coseismic displacement suggest that the northeastern study area was primarily subjected to shear stress, whereas the southwestern region experienced a combination of strike-slip and tensile stresses.

(4) The rupture of the 2023 Turkey earthquake doublet appears to have bridged a long-standing seismic gap, characterized by sparse seismic activity over the past 200 years. These observations suggest that further investigation is urgently needed to improve our understanding of the mechanisms of large earthquakes and to mitigate disasters in densely populated areas within continental collision zones.

Acknowledgments (Data and Resources)

We acknowledge the editor and two anonymous reviewers for their comments, which improved the quality of the manuscript. This research was supported by grants from the National Natural Science Foundation of China (Grant Nos. 42130312 and 41988101-01), and the Second Tibetan Plateau Scientific Expedition and Research Program (Grant No. 2019QZKK07). The focal mechanisms were obtained from the gCMT (https://www.globalcmt.org/CMTsearch.html, last accessed June 2023) and AFAD (https://deprem.afad.gov.tr/event-focal-mechanism, last accessed June 2023). The earthquake catalog and arrival time data were acquired

from AFAD (https://deprem.afad.gov.tr/event-catalog, last accessed June 2023). The coseismic offset measurements of GNSS for the 2023 Turkey earthquake doublet are available from the NGL (http://geodesy.unr.edu/, last accessed October 2023; http://geodesy.unr.edu/news_items/20230213/us6000jllz_final5min.txt; http://geodesy.unr.edu/news_items/20230213/us6000-jlqa_final5min.txt). The catalog for large earthquakes with $M_W \geq 5.0$ were downloaded from Utsu (2002), the USGS (https://earthquake.usgs.gov/earthquakes/search/, last accessed February 2023), and AFAD. The Generic Mapping Tools (GMT; Wessel et al., 2013) and Seis-PC (Ishikawa, 1986) software were used to plot some of the figures. The Supplemental Material includes seven figures and one table that supplement the main article.

References

Abdulnaby, W., Mahdi, H., Numan, N. M. S., and Al-Shukri, H. (2014). Seismotectonics of the Bitlis-Zagros fold and thrust belt in northern Iraq and surrounding regions from moment tensor analysis. *Pure Appl. Geophys.*, *171*(7), 1237–1250. https://doi.org/10.1007/s00024-013-0688-4

AFAD. (2023). Disaster and Emergency Management Authority, Turkey. https://deprem.afad.gov.tr/

Aktug, B., Ozener, H., Dogru, A., Sabuncu, A., Turgut, B., Halicioglu, K., Yilmaz, O., and Havazli, E. (2016). Slip rates and seismic potential on the East Anatolian Fault System using an improved GPS velocity field. *J. Geodyn., 94-95*, 1-12. https://doi.org/10.1016/j.jog.2016.01.001

Ambraseys, N. N. (1989). Temporary seismic quiescence: SE turkey. *Geophys. J. Int.*, *96*(2), 311–331. https://doi.org/10.1111/j.1365-246X.1989.tb04453.x

Bai, L., Liu, H. B., Ritsema, J., Mori, J., Zhang, T. Z., Ishikawa, Y., and Li, G. H. (2016). Faulting structure above the Main Himalayan Thrust as shown by relocated aftershocks of the 2015 M_W7.8 Gorkha, Nepal Earthquake. *Geophys. Res. Lett.*, *43*(2), 637–642. https://doi.org/10.1002/2015GL066473

Bai, L., Li, G. H., Khan, N. G., Zhao, J. M., and Ding, L. (2017). Focal depths and mechanisms of shallow earthquakes in the Himalayan-Tibetan region. *Gondwana Res.*, *41*, 390–399. https://doi.org/10.1016/j.gr.2015.07.009

Bai, L., Klemperer, S. L., Mori, J., Karplus, M. S., Ding, L., Liu, H. B., Li, G. H., Song, B. W., and Dhakal, S. (2019). Lateral variation of the Main Himalayan Thrust controls the rupture length of the 2015 Gorkha earthquake in Nepal. *Sci. Adv.*, *5*(6), eaav0723. https://doi.org/10.1126/sciadv.aav0723

Bilham, R., Gaur, V. K., and Molnar, P. (2001). Himalayan seismic hazard. *Science*, *293*(5534), 1442–1444. https://doi.org/10.1126/science.1062584

Bilham, R. (2019). Himalayan earthquakes: a review of historical seismicity and early 21st century slip potential. *Geolog. Soc., London, Spec. Publicat., 483*(1), 423–482. https://doi.org/10.1144/SP483.16

Chen, W. K., Rao, G., Kang, D. J., Wan, Z. F., and Wang, D. (2023). Early report of the source characteristics, ground motions, and casualty estimates of the 2023 M_W 7.8 and 7.5 Turkey earthquakes. *J. Earth Sci.*, *34*(2), 297–303. https://doi.org/10.1007/s12583-023-1316-6

Claerbout, J. F. (1976). *Fundamentals of Geophysical Data Processing: With Applications to Petroleum Prospecting*. New York: McGraw-Hill.

Cui, H. W., Zheng, J. C., Wan, Y. G., Cheng, Y. H., Yang, F., Sun, Q. S., Zhao, R., Xu, X., and Chai, G. B. (2022). The seismogenic structure of the 2021 Yunnan Yangbi M_S6.4 earthquake sequence and the difference between the Eryuan earthquake in 2013, Yangbi earthquake in 2017 and 2021. Chin. *J. Geophys. (in Chinese)*, *65*(2), 620–636. https://doi.org/10.6038/cjg2022P0425

Dal Zilio, L., and Ampuero, J. P. (2023). Earthquake doublet in Turkey and Syria. *Commun. Earth Environ.*, *4*(1), 71. https://doi.org/10.1038/s43247-023-00747-z

Delph, J. R., Biryol, C. B., Beck, S. L., Zandt, G., and Ward, K. M. (2015). Shear wave velocity structure of the Anatolian Plate: Anomalously slow crust in southwestern Turkey. *Geophys. J. Int.*, *202*(1), 261–276. https://doi.org/10.1093/gji/ggv141

Ding, H. Y., Zhou, Y. J., Ge, Z. X., Taymaz, T., Ghosh, A., Xu, H. Y., Irmak, T. S., and Song, X. D. (2023). High-resolution seismicity imaging and early aftershock migration of the 2023 Kahramanmaraş (SE Türkey) M_W7.9 & 7.8 earthquake doublet. *Earthq. Sci.*, *36*(6), 417–432. https://doi.org/10.1016/j.eqs.2023.06.002

Dziewonski, A. M., Chou, T. A., and Woodhouse, J. H. (1981). Determination of earthquake source parameters from waveform data for studies of global and regional seismicity. *J. Geophys. Res.: Solid Earth*, *86*(B4), 2825–2852. https://doi.org/10.1029/JB086iB04p02825

Ekström, G., Nettles, M., and Dziewoński, A. M. (2012). The global CMT project 2004-2010: centroid-moment tensors for 13,017 earthquakes. *Phys. Earth Planet. Inter., 200–201*, 1–9. https://doi.org/10.1016/j.pepi.2012.04.002

Erdik, M., Tümsa, M. B. D., Pınar, A., Altunel, E., and Zülfikar, A. C. (2023). A preliminary report on the February 6, 2023 earthquakes in Türkiye. https://doi.org/10.32858/temblor.297

Gephart, J. W., and Forsyth, D. W. (1984). An improved method for determining the regional stress tensor using earthquake focal mechanism data: application to the San Fernando earthquake sequence. *J. Geophys. Res.: Solid Earth*, *89*(B11), 9305–9320. https://doi.org/10.1029/JB089iB11p09305

Guiraud, M., Laborde, O., and Philip, H. (1989). Characterization of various types of deformation and their corresponding deviatoric stress tensors using microfault analysis. *Tectonophysics*, *170*(3-4), 289–316. https://doi.org/10.1016/0040-1951(89)90277-1

Hall, S. (2023). What Turkey's earthquake tells us about the science of seismic forecasting. *Nature*, *615*(7952), 388–389. https://doi.org/10.1038/d41586-023-00685-y

Hardebeck, J. L., and Michael, A. J. (2006). Damped regional-scale stress inversions: methodology and examples for southern California and the Coalinga aftershock sequence. *J. Geophys. Res.: Solid Earth*, *111*(B11), B11310. https://doi.org/10.1029/2005JB004144

Hatzfeld, D., and Molnar, P. (2010). Comparisons of the kinematics and deep structures of the Zagros and Himalaya and of the Iranian and Tibetan plateaus and geodynamic implications. *Rev. Geophys.*, *48*(2), RG2005. https://doi.org/10.1029/2009RG000304

Huang, J. C., Wan, Y. G., Sheng, S. Z., Li, X., and Gao, X. W. (2016). Heterogeneity of present-day stress field in the Tonga–Kermadec subduction zone and its geodynamic significance. *Chin. J. Geophys. (in Chinese)*, *59*(2), 578–592. https://doi.org/10.6038/cjg20160216

Ishikawa, Y. (1986). Introduction to the revision of SEIS-PC. *Geol. Inf. (in Japanese)*, *11*, 65–74.

Jia, Z., Jin, Z. Y., Marchandon, M., Ulrich, T., Gabriel, A. A., Fan, W. Y., Shearer, P., Zou, X. Y., Rekoske, J., … Fialko, Y. (2023). The complex dynamics of the 2023 Kahramanmaraş, Turkey, M_W7.8-7.7 earthquake doublet. *Science*, *381*(6661), 985–990. https://doi.org/10.1126/science.adi0685

Karabacak, V., Özkaymak, Ç., Sözbilir, H., Tatar, O., Aktuğ, B., Özdağ, Ö. C., Çakir, R., Aksoy, E., Koçbulut, F., … Arslan, G. (2023). The 2023 Pazarcık (Kahramanmaraş, Türkiye) earthquake (M_W 7.7): implications for surface rupture dynamics along the East Anatolian Fault Zone. *J. Geol. Soc.*, *180*(3), jgs2023–020. https://doi.org/10.1144/jgs2023-020

Karabulut, H., Güvercin, S. E., Hollingsworth, J., and Konca, A. Ö. (2023). Long silence on the East Anatolian Fault Zone (Southern Turkey) ends with devastating double earthquakes (6 February 2023) over a seismic gap: Implications for the seismic potential in the eastern Mediterranean region. *J. Geol. Soc.*, *180*(3), jgs2023–021. https://doi.org/10.1144/jgs2023-021

Khattri, K. N. (1987). Great earthquakes, seismicity gaps and potential for earthquake disaster along the Himalaya plate boundary. *Tectonophysics*, *138*(1), 79–92. https://doi.org/10.1016/0040-1951(87)90067-9

Laske, G., Masters, G., Ma, Z., and Pasyanos, M. (2013). Update on CRUST 1.0—A 1-degree global model of Earth's crust. *Geophysical Research Abstracts, 15*, Abstract EGU2013-2658. http://igppweb.ucsd.edu/~gabi/rem.html

Li, D. H., Ding, Z. F., Zhan, Y., Wu, P. P., Chang, L. J., and Sun, X. Y. (2021). Upper crustal velocity and seismogenic environment of the *M*7.0 Jiuzhaigou earthquake region in Sichuan, China. *Earth Planet. Phys.*, *5*(4), 348–361. https://doi.org/10.26464/epp2021038

Li, S. P., Wang, X., Tao, T. Y., Zhu, Y. C., Qu, X. C., Li, Z. X., Huang, J. W., and Song, S. Y. (2023). Source Model of the 2023 Turkey Earthquake sequence imaged by sentinel-1 and GPS measurements: implications for heterogeneous fault behavior along the East Anatolian Fault Zone. *Remote Sens.*, *15*(10), 2618. https://doi.org/10.3390/rs15102618

Lloyd, R. (2014). Evaluating the style of continental deformation in eastern Turkey using InSAR and GPS. Reinvention: An international Journal of

Undergraduate Research, BCUR 2014 Special Issue. http://www.warwick.ac.uk/reinventionjournal/archive/bcur2014specialissue/lloyd

Lund, B., and Townend, J. (2007). Calculating horizontal stress orientations with full or partial knowledge of the tectonic stress tensor. *Geophys. J. Int.*, *170*(3), 1328–1335. https://doi.org/10.1111/j.1365-246X.2007.03468.x

Manighetti, I., Mercier, A., and De Barros, L. (2021). Fault trace corrugation and segmentation as a measure of fault structural maturity. *Geophys. Res. Lett.*, *48*(20), e2021GL095372. https://doi.org/10.1029/2021GL095372

Martínez-Garzón, P., Kwiatek, G., Ickrath, M., and Bohnhoff, M. (2014). MSATSI: a MATLAB package for stress inversion combining solid classic methodology, a new simplified user-handling, and a visualization tool. *Seismol. Res. Lett.*, *85*(4), 896–904. https://doi.org/10.1785/0220130189

Melgar, D., Ganas, A., Taymaz, T., Valkaniotis, S., Crowell, B. W., Kapetanidis, V., Tsironi, V., Yolsal-Çevikbilen, S., and Öcalan, T. (2020). Rupture kinematics of 2020 January 24 M_W 6.7 Doğanyol-Sivrice, Turkey earthquake on the East Anatolian Fault Zone imaged by space geodesy. *Geophys. J. Int.*, *223*(2), 862–874. https://doi.org/10.1093/gji/ggaa345

Melgar, D., Taymaz, T., Ganas, A., Crowell, B., Öcalan, T., Kahraman, M., Tsironi, V., Yolsal-Çevikbilen, S., Valkaniotis, S., … Altuntaş, C. (2023). Sub- and super-shear ruptures during the 2023 $\mathrm{M_W}$ 7.8 and $\mathrm{M_W}$ 7.6 earthquake doublet in SE Türkiye. *Seismica, 2*(3). https://doi.org/10.26443/seismica.v2i3.387

Meng, J. N., Kusky, T., Mooney, W. D., Bozkurt, E., Bodur, M. N., and Wang, L. (2024). Surface deformations of the 6 February, 2023 earthquake sequence, eastern Türkiye. *Science*, *383*(6680), 298–305. https://doi.org/10.1126/science.adj3770

Mutlu, A. K., and Karabulut, H. (2011). Anisotropic Pn tomography of Turkey and adjacent regions. *Geophys. J. Int.*, *187*(3), 1743–1758. https://doi.org/10.1111/j.1365-246X.2011.05235.x

Naddaf, M. (2023). Turkey–Syria earthquake: what scientists know. *Nature*, *614*(7948), 398–399. https://doi.org/10.1038/d41586-023-00364-y

Okuwaki, R., Yagi, Y., Taymaz, T., and Hicks, S. P. (2023). Multi-scale rupture growth with alternating directions in a complex fault network during the 2023 South-eastern Türkiye and Syria earthquake doublet. *Geophys. Res. Lett.*, *50*(12), e2023GL103480. https://doi.org/10.1029/2023GL103480

Över, S., Ünlügenç, U. C., and Bellier, O. (2002). Quaternary stress regime change in the Hatay region (SE Turkey). *Geophys. J. Int.*, *148*(3), 649–662. https://doi.org/10.1046/j.1365-246X.2002.01621.x

Perrin, C., Manighetti, I., Ampuero, J. P., Cappa, F., and Gaudemer, Y. (2016). Location of largest earthquake slip and fast rupture controlled by along-strike change in fault structural maturity due to fault growth. *J. Geophys. Res.: Solid Earth*, *121*(5), 3666–3685. https://doi.org/10.1002/2015JB012671

Rahman, M. M., and Bai, L. (2018). Probabilistic seismic hazard assessment of Nepal using multiple seismic source models. *Earth Planet. Phys.*, *2*(4), 327–341. https://doi.org/10.26464/epp2018030

Reilinger, R., McClusky, S., Vernant, P., Lawrence, S., Ergintav, S., Cakmak, R., Ozener, H., Kadirov, F., Guliev, I., … Karam1, G. (2006). GPS constraints on continental deformation in the Africa-Arabia-Eurasia continental collision zone and implications for the dynamics of plate interactions. *J. Geophys. Res.: Solid Earth*, *111*(B5), B05411. https://doi.org/10.1029/2005JB004051

Ren, C. M., Wang, Z. X., Taymaz, T., Hu, N., Luo, H., Zhao, Z. Y., Yue, H., Song, X. D., Shen, Z. K., … Ding. H. Y. (2024). Supershear triggering and cascading fault ruptures of the 2023 Kahramanmaraş, Türkiye earthquake doublet. *Science*, *383*(6680), 305–311. https://doi.org/10.1126/science.adi1519

Sandvol, E., Turkelli, N., and Barazangi, M. (2003). The Eastern Turkey Seismic Experiment: the study of a young continent–continent collision. *Geophys. Res. Lett.*, *30*(24), 8038. https://doi.org/10.1029/2003GL018912

Shao, X. H., Yao, H. J., Liu, Y., Yang, H. F., Tian, B. F., and Fang, L. H. (2022). Shallow crustal velocity structures revealed by active source tomography and fault activities of the Mianning–Xichang segment of the Anninghe fault zone, Southwest China. *Earth Planet. Phys.*, *6*(2), 204–212. https://doi.org/10.26464/epp2022010

Styron, R., and Pagani, M. (2020). The GEM global active faults database. *Earthq. Spectra*, *36*(S1), 160–180. https://doi.org/10.1177/8755293020944182

Taymaz, T., Ganas, A., Yolsal-Çevikbilen, S., Vera, F., Eken, T., Erman, C., Keleş, D., Kapetanidis, V., Valkaniotis, S., … Ocalan, T. (2021). Source mechanism and rupture process of the 24 January 2020 M_W 6.7 Doğanyol–Sivrice Earthquake obtained from seismological waveform analysis and space geodetic observations on the East Anatolian Fault Zone (Turkey). *Tectonophysics*, *804*, 228745. https://doi.org/10.1016/j.tecto.2021.228745

Tian, J. H., Luo, Y., and Zhao, L. (2019). Regional stress field in Yunnan revealed by the focal mechanisms of moderate and small earthquakes. *Earth Planet. Phys.*, *3*(3), 243–252. https://doi.org/10.26464/epp2019024

Utsu, T. (2002). A list of deadly earthquakes in the world: 1500-2000. Int. *Geophys.*, *81*, 691–717. https://doi.org/10.1016/s0074-6142(02)80245-5

Waldhauser, F., and Ellsworth, W. L. (2000). A double-difference earthquake location algorithm: method and application to the northern Hayward Fault, California. *Bull. Seismol. Soc. Am.*, *90*(6), 1353–1368. https://doi.org/10.1785/0120000006

Wan, Y. G., Sheng, S. Z., Huang, J. C., Li, X., and Chen, X. (2016). The grid search algorithm of tectonic stress tensor based on focal mechanism data and its application in the boundary zone of China, Vietnam and Laos. *J. Earth Sci.*, *27*(5), 777–785. https://doi.org/10.1007/s12583-015-0649-1

Wang, H. B., Huang, Z. C., Eken, T., Keleş, D., Kaya-Eken, T., Confal, J. M., Erman, C., Yolsal-Çevikbilen, S., Zhao, D. P., and Taymaz, T. (2020). Isotropic and anisotropic *P* wave velocity structures of the crust and uppermost mantle beneath Turkey. *J. Geophys. Res.: Solid Earth*, *125*(12), e2020JB019566. https://doi.org/10.1029/2020JB019566

Warren, L. M., Beck, S. L., Biryol, C. B., Zandt, G., Özacar, A. A., and Yang, Y. J. (2013). Crustal velocity structure of Central and Eastern Turkey from ambient noise tomography. *Geophys. J. Int.*, *194*(3), 1941–1954. https://doi.org/10.1093/gji/ggt210

Wessel, P., Smith, W. H. F., Scharroo, R., Luis, J., and Wobbe, F. (2013). Generic mapping tools: improved version released. *EOS Trans.*, *94*(45), 409–410. https://doi.org/10.1002/2013EO450001

Xiao, Z., and Gao, Y. (2017). Crustal velocity structure beneath the northeastern Tibetan plateau and adjacent regions derived from double difference tomography. *Chin. J. Geophys. (in Chinese)*, *60*(6), 2213–2225. https://doi.org/10.6038/jg20170615

Xu, C. Y., Zhang, Y., Hua, S. B., Zhang, X., Xu, L. S., Chen, Y. T., and Taymaz, T. (2023). Rapid source inversions of the 2023 SE Türkiye earthquakes with teleseismic and strong-motion data. *Earthq. Sci.*, *36*(4), 316–327. https://doi.org/10.1016/j.eqs.2023.05.004

Yao, H. J. (2012). Lithospheric structure and deformation in SE Tibet revealed by ambient noise and earthquake surface wave tomography: recent advances and perspectives. *Earthq. Sci.*, *25*(5-6), 371–383. https://doi.org/10.1007/s11589-012-0863-1

Yilmaz, H., Over, S., and Ozden, S. (2006). Kinematics of the East Anatolian Fault Zone between Turkoglu (Kahramanmaras) and Celikhan (Adiyaman), eastern Turkey. *Earth Planets Space, 58*(11), 1463-1473. https://doi.org/10.1186/BF03352645

Zhan, H. L., Bai, L., and Chen, Z. W. (2023). Source parameters, seismogenic structures of the 1950 Medog–Zayu M_S8.6 earthquake and seismicity in the surrounding areas. *Rev. Geophys. Planet. Phys. (in Chinese)*, *54*(1), 44–55. https://doi.org/10.19975/j.dqyxx.2022-020

Zhang, H. J., and Thurber, C. H. (2003). Double-difference tomography: the method and its application to the Hayward fault, California. *Bull. Seismol. Soc. Am.*, *93*(5), 1875–1889. https://doi.org/10.1785/0120020190

Zhang, H. J., and Thurber, C. (2006). Development and applications of double-difference seismic tomography. *Pure Appl. Geophys.*, *163*(2-3), 373–403. https://doi.org/10.1007/s00024-005-0021-y

Zhang, Y. J., Tang, X. W., Liu, D. C., Taymaz, T., Eken, T., Guo, R. M., Zheng, Y., Wang, J. Q., and Sun, H. P. (2023). Geometric controls on cascading rupture of the 2023 Kahramanmaraş earthquake doublet. *Nat. Geosci.*, *16*(11), 1054–1060. https://doi.org/10.1038/s41561-023-01283-3

Zhou, S. Y., and Xu, Z. H. (2018). *Textbook on Modern Seismology* (2nd ed) (in Chinese). Beijing: Peking University Press.

Zor, E., Sandvol, E., Gürbüz, C., Türkelli, N., Seber, D., and Barazangi, M. (2003). The crustal structure of the East Anatolian plateau (Turkey) from receiver functions. *Geophys. Res. Lett.*, *30*(24), 8044. https://doi.org/10.1029/2003GL018192

Supplementary Materials for "The 2023 Turkey earthquake doublet: earthquake relocation, seismic tomography and stress field inversion"

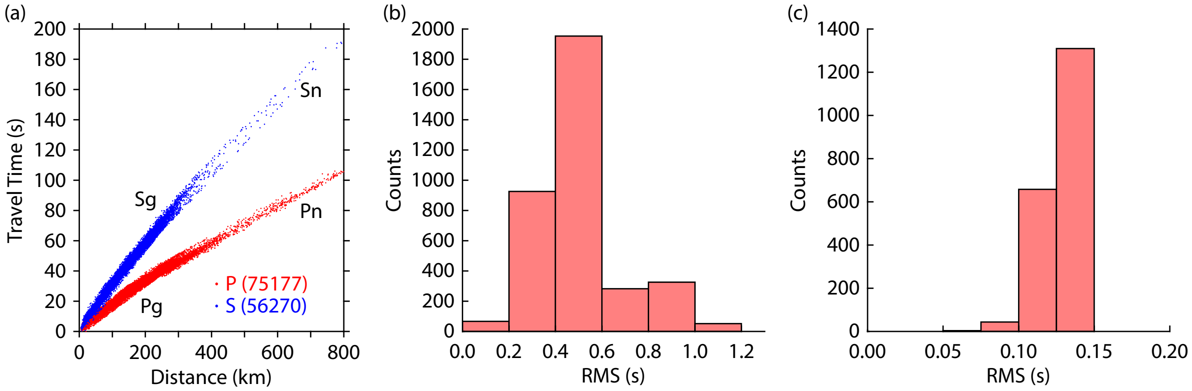

Figure S1. Fitting diagram of time-distance curve and histograms of travel time residual RMS. (a) Arrival times of direct (Pg and Sg) and head (Pn and Sn) waves vs. epicentral distances for all 3707 earthquakes. (b) Travel time residual RMS before earthquake relocation. (c) Travel time residual RMS after earthquake relocation.

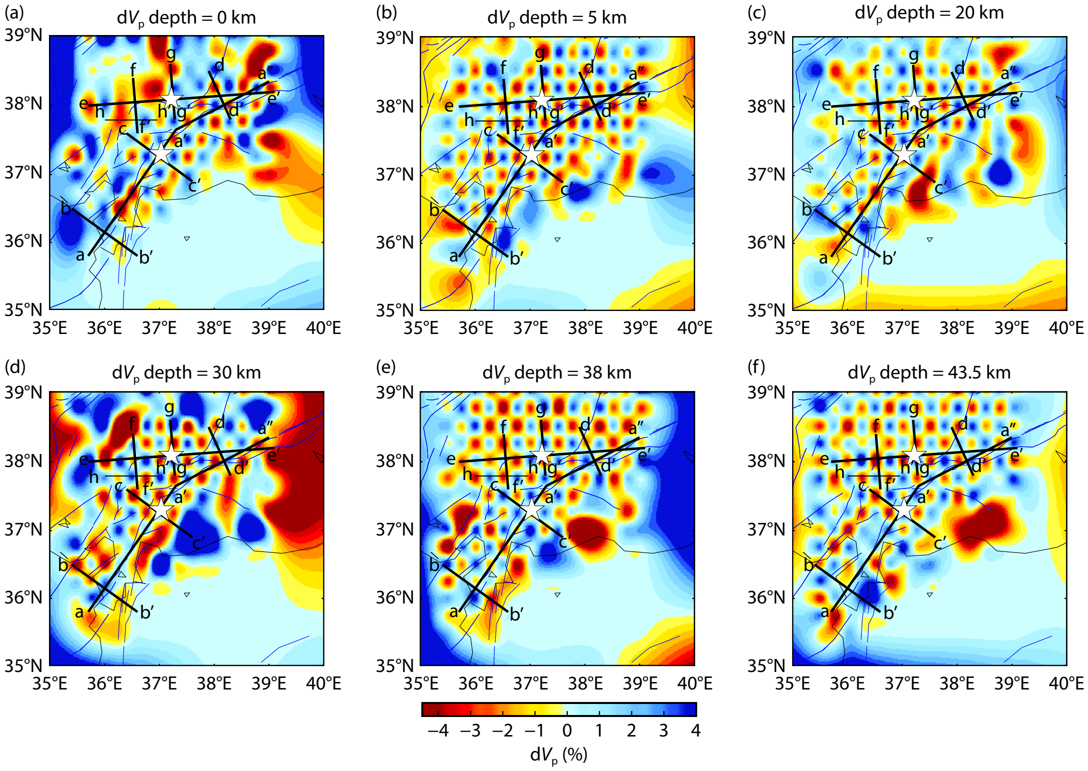

Figure S2. The checkerboard test for P-wave velocity anomalies horizontal at different depths. At the top of each map, the layer depth is given: (a) 0, (b) 5, (c) 20, (d) 30, (e) 38, and (f) 43.5 km. The thin lines are active faults. The thick lines are the profile lines a–a′–a″, b–b′, c–c′, d–d′, e–e′, f–f′, g–g′, h–h′.

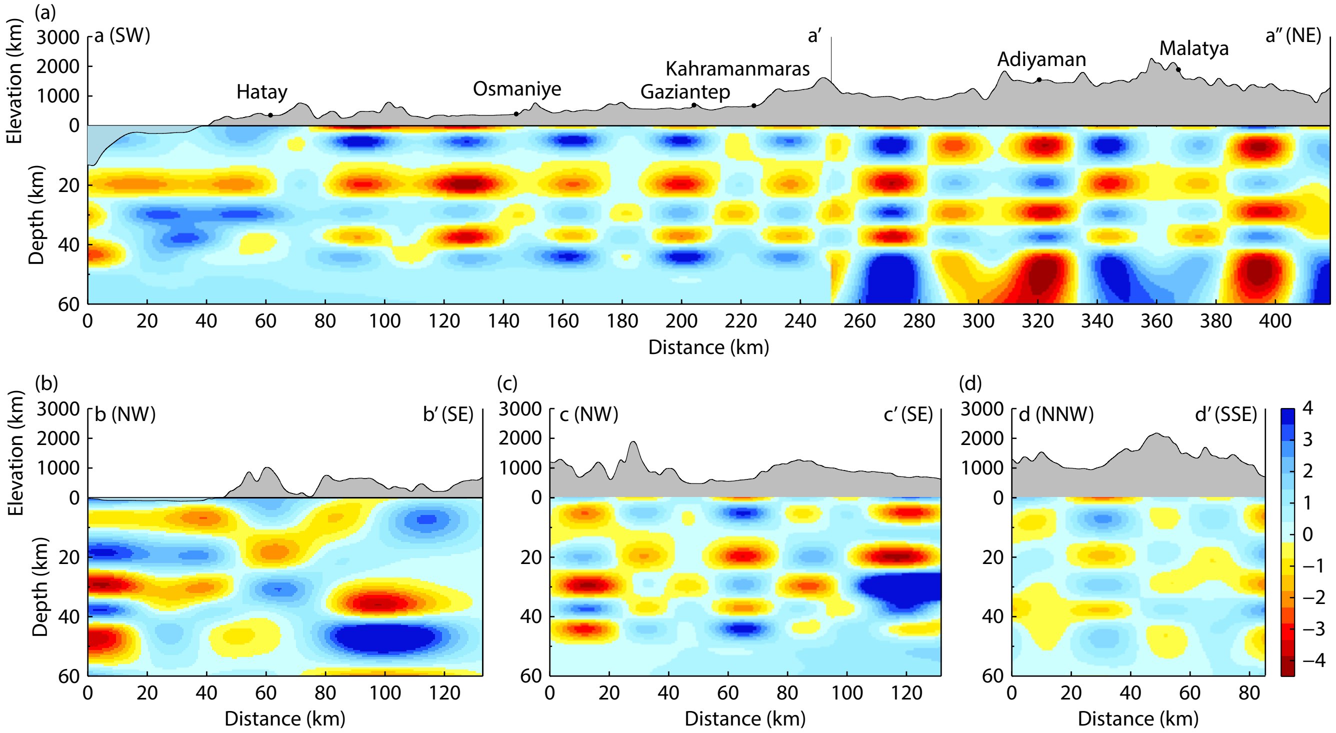

Figure S3. The checkerboard test for the P-wave velocity at vertical profiles based on Figure 3.

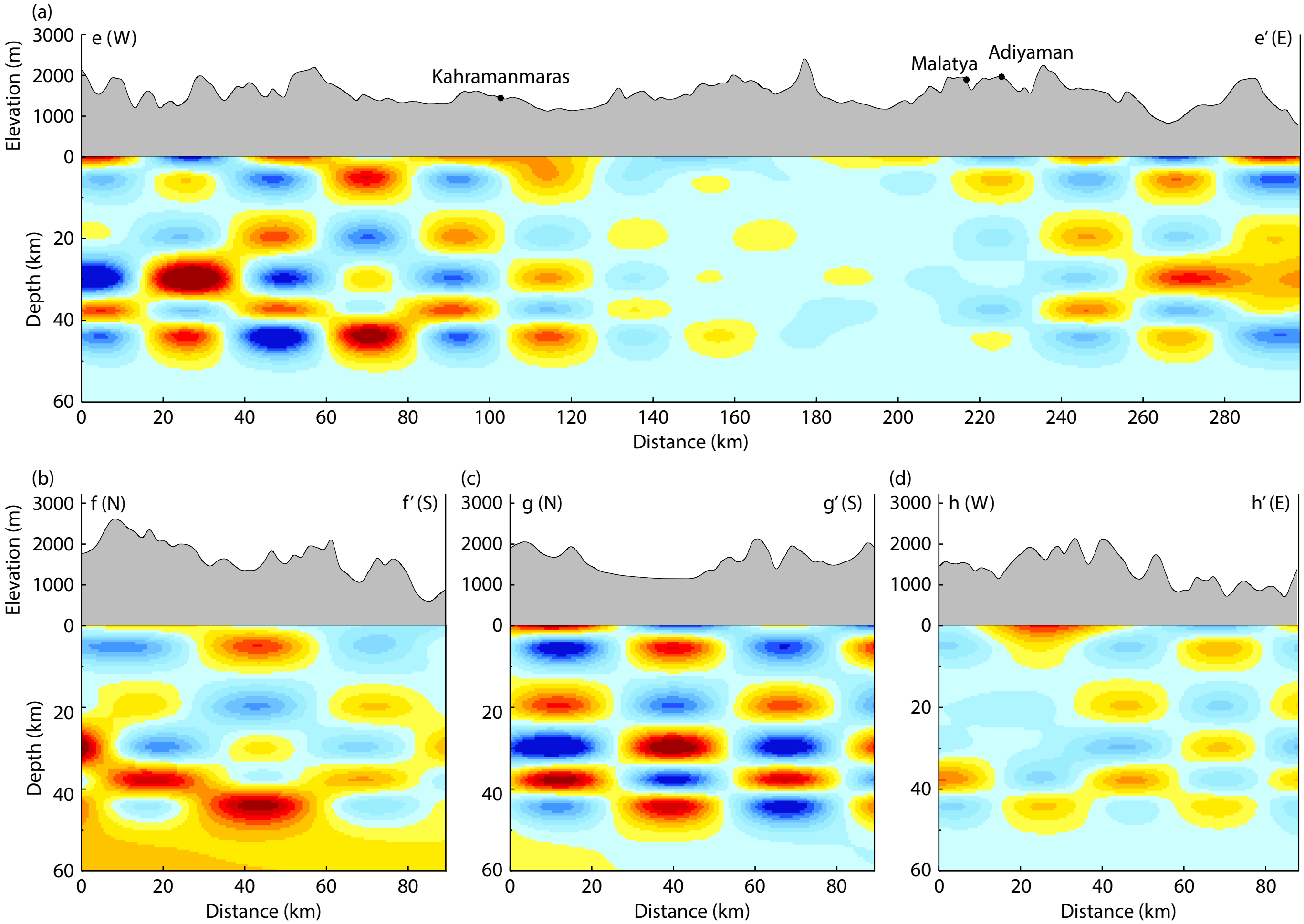

Figure S4. The checkerboard test for the P-wave velocity at vertical profiles based on Figure 4.

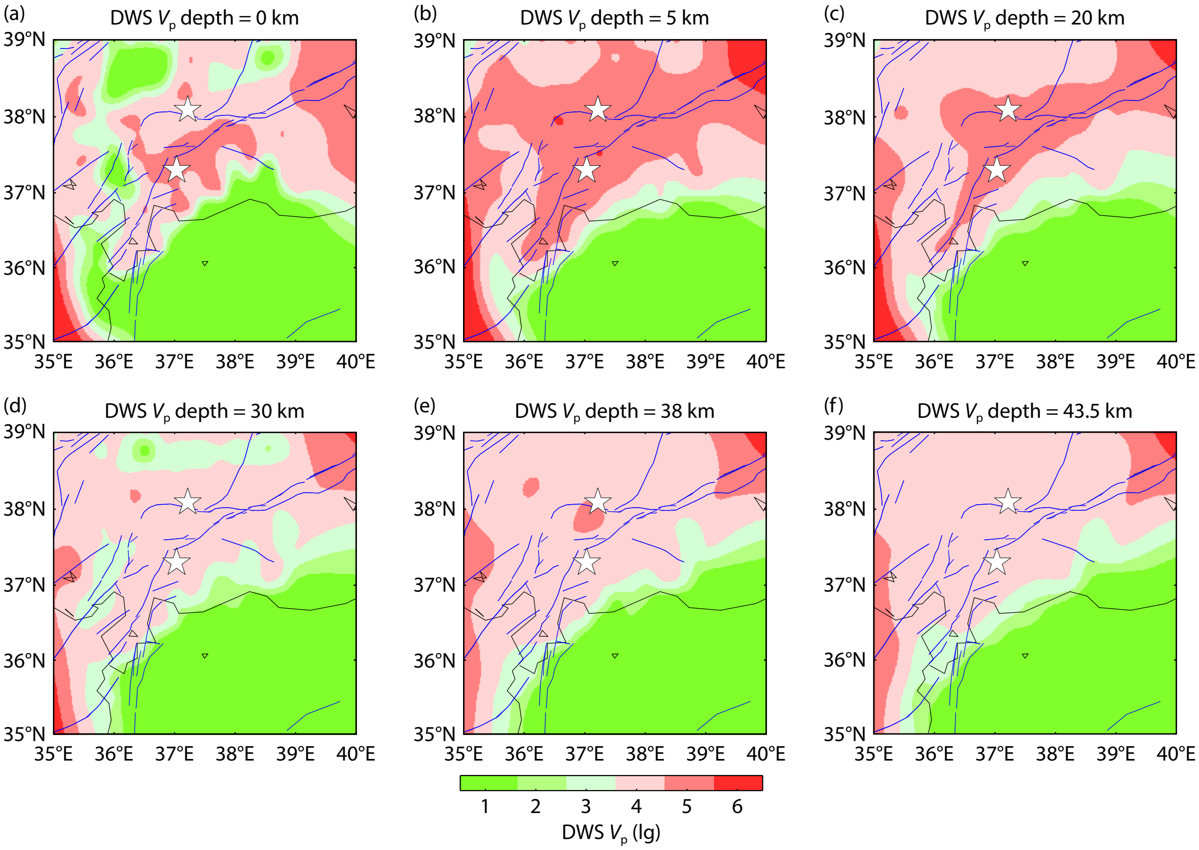

Figure S5. The DWS distribution of the P-wave ray path at different depths. The symbols are the same as in Figure S2.

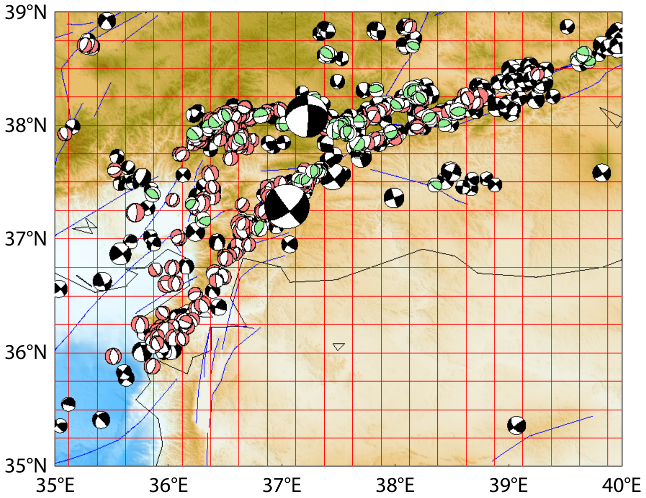

Figure S6. Distribution of earthquakes and grid cells that used to calculate the tectonic stress field. Pink beachballs represent the normal faulting mechanisms, light green beachballs represent the thrust faulting mechanisms, black beachballs represent the strike-slip faulting mechanisms. The red straight lines indicate the grid lines for the stress field calculation.

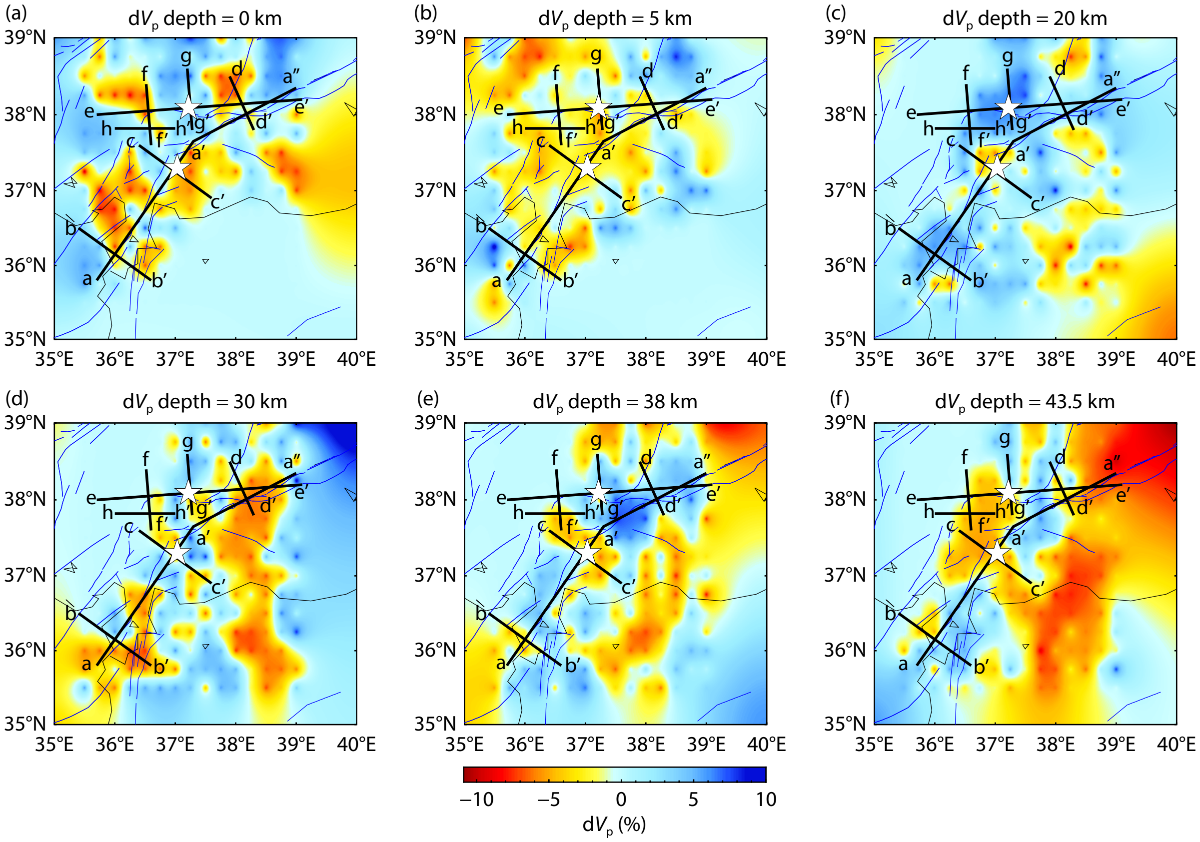

Figure S7. Results of P-wave velocity anomalies at different depths. The symbols are the same as in Figure S2.

Table S1. Focal mechanisms of 14 earthquakes with $M_w \geq 5.5$ (Dziewonski et al., 1981; Ekström et al., 2012; AFAD, 2023).

No.	Time (UTC)	Lon (°E)	Lat (°N)	Mag.	Depth (km)	Strike (°)	Dip (°)	Rake (°)	Reference	No. in Figure 2
1	2023.2.6 1:18:11	37.0322	37.2991	7.8	11.08	51	70	−4	gCMT	6
2	2023.2.6 1:26:49	36.9605	37.2231	5.6	8.57	200	81	−22	AFAD	4
3	2023.2.6 1:28:16	36.9131	37.2975	6.6	10.44	187	43	−30	AFAD	5
4	2023.2.6 1:36:28	36.6641	37.1263	5.7	9.18	254	45	−52	AFAD	3
5	2023.2.6 2:3:35	37.9671	37.9497	5.6	12.16	241	56	31	AFAD	8
6	2023.2.6 10:24:59	37.2166	38.0922	7.5	12.32	264	46	−9	gCMT	10
7	2023.2.6 10:32:8	37.2560	38.0867	5.5	14.97	75	78	23	AFAD	11
8	2023.2.6 10:35:57	37.9202	38.1816	5.9	15.70	31	31	32	AFAD	12
9	2023.2.6 10:51:30	38.1287	38.2624	5.7	4.43	41	58	79	AFAD	13
10	2023.2.6 12:2:11	36.4845	38.0687	5.9	10.84	9	56	−95	AFAD	9
11	2023.2.6 20:37:51	37.0320	37.3205	5.5	14.38	171	49	−74	AFAD	7
12	2023.2.20 17:4:27	36.0955	36.0980	6.4	14.43	214	57	−44	AFAD	1
13	2023.2.20 17:7:34	35.9646	36.1986	5.8	10.90	187	24	−95	AFAD	2
14	2023.2.27 9:4:49	38.2385	38.2658	5.6	13.53	353	62	163	AFAD	14